Fundamentals of cavity-enhanced polarimetry for parity-nonconserving optical rotation measurements: Application to Xe, Hg, and I

L. Bougas,[1,2] G. E. Katsoprinakis,[1] W. von Klitzing,[1] and T. P. Rakitzis[1,2,*]

[1]*Institute of Electronic Structure and Laser, Foundation for Research and Technology–Hellas, 71110 Heraklion-Crete, Greece*
[2]*Department of Physics, University of Crete, 71003 Heraklion-Crete, Greece*

We present the theoretical basis of a cavity-enhanced polarimetric scheme for the measurement of parity-nonconserving (PNC) optical rotation. We discuss the possibility of detecting PNC optical rotation in accessible transitions in metastable Xe and Hg and ground-state I. In particular, the physics of the PNC optical rotation is presented and we explore the line-shape effects on the expected PNC optical rotation signals. Furthermore, we present an analysis of the eigenpolarizations of the cavity-enhanced polarimeter, which is necessary for understanding the measurement procedure and the ability of employing robust background subtraction procedures using two signal reversals. Using recent atomic structure theoretical calculations, we present simulations of the PNC optical rotation signals for all proposed transitions, assuming a range of experimentally feasible parameters. Finally, the possibility of performing sensitive measurements of the nuclear-spin-dependent PNC effects is investigated for the odd-neutron nuclei ^{129}Xe and ^{199}Hg and the odd-proton nucleus ^{127}I.

PACS number(s): 11.30.Er, 12.15.Mm, 07.60.Fs

I. INTRODUCTION

The possibility of measuring parity nonconservation (PNC) in atoms was first considered by Zel'dovich in 1959 [1]. However, atomic PNC experiments began only after Bouchiat and Bouchiat showed that parity mixing of atomic states scales as $\sim Z^3$ and measurable signals could be obtained for high-Z atoms [2]. For high Z, the degree of s-p parity mixing, in some atomic states, is of order 10^{-12}–10^{-10}. The precise measurement of this atomic PNC can provide a stringent low-energy test of the standard model [3], internucleon weak interactions, and nuclear structure [4].

There are several methods in which the parity mixing can be measured and for each method the optimal atomic candidates are usually different. For example, the Stark interference technique has been used to measure PNC in Cs [5], Yb [6], and Dy [7] and proposed for Fr [8] and Rb [9,10]; the optical rotation technique has been used successfully for Tl [11], Bi [12], and Pb [13]; the ac Stark shift method has been proposed for Ba$^+$ [14] and Ra$^+$ [15,16] ions; and the hyperfine transition method has been proposed for K [17], Rb [9], and Fr [18]. To date, the most successful atomic PNC measurement has been the 0.35% precision measurement of nuclear-spin-independent PNC in Cs [5]. As the precision in the atomic theory of other PNC candidates is not expected to significantly surpass the theoretical precision of Cs, current experiments are aiming at other important goals that are not dependent on extremely precise atomic theory calculations. Examples include the measurement of atomic PNC on a chain of isotopes [19,20] and the measurement of nuclear-spin-dependent effects in atomic systems (see Ref. [4] and references therein) and in molecules [21]. Therefore, along these lines, PNC experiments are in progress as mentioned above [6,7,14,16].

Due to the difficulty of controlling all the relevant parameters to the required precision, there have been only a handful of successful atomic PNC measurements and even the few successful experiments have typically required 10–20 years to yield precise results [5,6,11]. In addition, some of the current atomic PNC experiments are no longer tabletop, as they are performed on radioactive isotopes with short half-lives of a few minutes, such as on Fr at TRIUMF [18] and Ra$^+$ at KVI [15,16].

Recently, our group has proposed an extension of the optical-rotation technique, with the use of a bow-tie optical cavity [22]. We show in detail that the proposed cavity-enhanced technique produces large experimental optical-rotation signals and robust experimental checks and allows different atomic candidates to be considered. Specifically, our proposal has several potential advantages, which solve some of the problems of past PNC optical-rotation experiments. These advantages include the following.

(a) The effective optical-rotation path length is enhanced using a high-finesse cavity by $2\mathcal{F}/\pi$, where $\mathcal{F}$ is the finesse of the cavity (for high-finesse cavities $\mathcal{F} \sim 10^4$–10^5), allowing the study of PNC in atomic systems for which single-pass optical rotation from available column densities is otherwise too small. We focus on metastable states in Hg and Xe [22] and ground-state I atoms [23], for which the single-pass optical rotation from available column densities requires enhancement of between 10^2 and 10^4 cavity passes to produce measurable signals. In addition, the proposed atomic systems are compatible with a high-finesse optical cavity, as high atomic densities can be produced at around room temperature (for the case of Tl, Bi, and Pb, temperatures in excess of 1000 K were required, which is difficult to combine with high-transmission windows and a stable optical cavity).

(b) Two signal reversals are introduced. The main limitation in the original optical-rotation experiments was the lack of rapid subtraction procedures or signal reversals. The proposed signal reversals are effected either by inverting the longitudinal magnetic field in the cavity or by shifting the cavity resonance to an opposite polarization mode. These signal reversals can be performed at a high repetition rate and allow the absolute optical rotation to be measured, without needing to remove the gas sample from the cavity. In addition, as metastable Hg and

---

*ptr@iesl.forth.gr

Xe and ground-state I can be produced by optical pumping, photodissociation, or electrical discharge, the concentration of these species can be varied very quickly, giving an additional rapid subtraction procedure.

(c) Of the proposed PNC candidates, both Hg and Xe have several, commercially available, stable isotopes. In addition, Hg and Xe each have two isotopes with an odd-neutron nucleus (^{199}Hg and ^{201}Hg and ^{129}Xe and ^{131}Xe, respectively). Moreover, iodine has a radioactive isotope ^{129}I, which can be commercially obtained. Both I isotopes have an odd-proton nucleus. Therefore, nuclear-spin-dependent effects can be measured for both odd-neutron and odd-proton nuclei, as well as PNC measurements along a chain of isotopes [19,20,24].

The aim of this paper is to explain the main features of the cavity-enhanced PNC optical-rotation scheme in depth and to present simulated experimental signals for Hg, Xe, and I. In Sec. II we describe in brief the origin of the PNC optical rotation. In Sec. III we introduce the atomic systems considered for future PNC investigations using the cavity-enhanced optical-rotation technique and we examine the experimental feasibility of PNC measurements in these atomic systems. In Sec. IV we describe the properties of the cavity-enhanced scheme and derive the eigenmodes of a bow-tie cavity with circular birefringence (Faraday rotation and PNC optical rotation) and linear birefringence and discuss how the signal reversals are implemented. Finally, in Sec. V we simulate the PNC line shapes for several transitions in Hg, Xe, and I for a range of experimental conditions and discuss the results.

II. PARITY-NONCONSERVATION OPTICAL ROTATION

In this section we present the physics of the PNC optical-rotation technique. We note that the equations appearing here are expressed in SI units and the presented formulas follow largely the structure of Refs. [25,26] with helpful material coming from Refs. [27–33]. In addition, the derivation of the PNC rotation angle also draws from Refs. [4,34,35].

A PNC neutral-current interaction between the electrons and the nucleus of an atom mixes the parity eigenstates of the atom. This PNC-induced mixing allows for a weak electric dipole transition, with amplitude E_1^{PNC}, between states of the same parity. The size of E_1^{PNC} increases approximately as $\sim Z^3$ and is inversely proportional to the energy difference between the states of opposite parity mixed by the weak interaction [2] and typically is of order $10^{-11} e\alpha_B$–$10^{-10} e\alpha_B$ (e is the charge of the electron and α_B the Bohr radius). Measurement of this small parity-nonconserving amplitude is achieved through its interference with a larger parity-conserving amplitude.

In a PNC optical-rotation experiment, the parity-conserving amplitude is an allowed magnetic dipole amplitude M_1. The interference between the dominant $M1$-allowed amplitude and the PNC-induced E_1^{PNC} amplitude leads to optical activity. The PNC-induced optical rotation φ_{PNC} arises due to the difference in the indices of refraction for left- and right-circularly polarized light in the vicinity of the magnetic dipole resonance

$$\varphi_{\mathrm{PNC}} = \frac{\omega l}{c} \frac{n'_+ - n'_-}{2} = \frac{\pi l}{\lambda}(n'_+ - n'_-), \qquad (1)$$

where l is the length of vapor, λ is the optical wavelength, ω is the optical frequency, and $n'_{\pm}$ are the real parts of the

refractive indices for left- and right-circularly polarized light, respectively (which are functions of the optical frequency ω).

A. The $M1$ magnetic dipole interaction

We assume a magnetic dipole interaction of a laser beam with an atomic vapor. Treating the transition as a damped oscillator with a damping factor Γ, the index of refraction can be put in the form

$$n = n' + i n'' = 1 + \frac{\pi \mu_0 e^2}{4 m \omega_0} \rho f \mathcal{L}(\omega - \omega_0), \qquad (2)$$

where m is the mass of the electron, μ_0 is the vacuum permeability, e is the electronic charge, ω_0 is the resonant transition frequency, ρ is the vapor density, f is the oscillator strength, and $\mathcal{L} = \mathcal{L}' + i\mathcal{L}''$ is the Lorentz line-shape function [given in Eqs. (A1) and (A2)]. Assuming that the transition is an isolated $J \to J'$ line without hyperfine structure, we have

$$f = \frac{2 m \omega_0}{3 \hbar e^2} \frac{M_1^2}{2J + 1}, \qquad (3)$$

where $M_1 \equiv \langle M_1 \rangle \equiv \langle J \| \mu^{(1)} \| J' \rangle$ is the reduced matrix element for the magnetic dipole operator $\mu^{(1)}$. Note that the magnetic dipole reduced matrix element M_1 will be the same for both states of circular polarization of the resonant laser field. Taking into account the Doppler broadening mechanism of the thermal vapor (see Appendix A) and using Eq. (3), we can put Eq. (2) in the form

$$n = 1 + \frac{\pi \mu_0}{2\hbar} \frac{\rho}{2J + 1} \frac{M_1^2}{3} \mathcal{V}(\omega - \omega_0), \qquad (4)$$

where $\mathcal{V} = \mathcal{V}' + i\mathcal{V}''$ is the Voigt profile function [given in Eqs. (A5) and (A6)].

To assume an atomic system with nonzero nuclear spin I we must take into account the hyperfine structure. Using

$$\langle F \| T^{(k)} \| F' \rangle = (-1)^{I+k+J+F'} \sqrt{(2F+1)(2F'+1)}$$
$$\times \begin{Bmatrix} J & k & J' \\ F' & I & F \end{Bmatrix} \langle J \| T^{(k)} \| J' \rangle, \qquad (5)$$

where k is the tensor rank of the operator T, and the fact that the population density of the ground hyperfine state F is very well approximated by

$$\rho(F) = \frac{2F + 1}{(2J + 1)(2I + 1)} \rho, \qquad (6)$$

then, from Eq. (4), by summing over final states and averaging over initial states we obtain

$$n = 1 + n_0 \sum_{F,F'} C_{FF'} \mathcal{V}_{FF'}(\omega), \qquad (7)$$

where we have defined

$$n_0 = \frac{\pi \mu_0}{2\hbar} \frac{\rho}{2J + 1} \frac{M_1^2}{3}, \qquad (8)$$

$$C_{FF'} = \frac{(2F+1)(2F'+1)}{2I+1} \begin{Bmatrix} J & 1 & J' \\ F' & I & F \end{Bmatrix}^2, \qquad (9)$$

and $\mathcal{V}_{FF'}(\omega) \equiv \mathcal{V}(\omega - \omega_{FF'})$ for a specific $F \to F'$ transition. Note that n_0 is not a dimensionless constant, but has units of angular frequency.

B. The $E1_{\mathrm{PNC}}$ electric dipole interaction

The PNC-induced optical rotation [Eq. (1)] results from the $M1$-$E1_{\mathrm{PNC}}$ interference, which leads to a difference in the indices of refraction for left- and right-circularly polarized light in the vicinity of the magnetic dipole resonance.

A circularly polarized laser beam (propagating along $\hat{z}$, for example) has electric- and magnetic-field vector components

$$E_\eta = -\frac{E(t)}{\sqrt{2}}(\hat{x} + i\eta\hat{y}), \quad B_\eta = \frac{B(t)}{\sqrt{2}}(i\eta\hat{x} - \hat{y}), \quad (10)$$

where $E(t)$ and $B(t)$ are the electric- and magnetic-field amplitudes of the laser's electric- and magnetic-field vectors, respectively, and $\eta = \pm 1$ denotes the two states of circular polarization (the positive sign corresponds to left-circularly polarized light).

Inclusion of the PNC-induced electric dipole amplitude and the magnetic dipole amplitude in the formulas for the index of refraction [Eqs. (7) and (8)] can be realized by performing the following substitution:

$$\frac{M_1^2}{3} \to \left| \langle J \| i d_\eta^{(1)} + \mu_\eta^{(1)} \| J' \rangle \right|^2, \quad (11)$$

where $d_\eta^{(1)}$ is the ηth component of the PNC electric dipole operator. The i in Eq. (11) ensures that $E_1^{\mathrm{PNC}} \equiv \langle E_1^{\mathrm{PNC}} \rangle \equiv \langle J \| i d^{(1)} \| J' \rangle$ violates parity but not time-reversal symmetry and therefore is purely imaginary [2].

From Eq. (11) it is now apparent that the transition rate will be different for right- and left-circularly polarized light [35]. Therefore, the difference between the refractive indices for left- (n_+) and right- (n_-) circularly polarized light will be different [Eq. (8)]. In particular, the difference between the n_+ and n_- will be proportional to

$$\frac{n_+ - n_-}{2(n-1)} = \frac{|E_1^{\mathrm{PNC}}E_+ + M_1 B_+|^2 - |E_1^{\mathrm{PNC}}E_- + M_1 B_-|^2}{|E_1^{\mathrm{PNC}}E_+ + M_1 B_+|^2 + |E_1^{\mathrm{PNC}}E_- + M_1 B_-|^2}$$
$$= \frac{i M_1 (E_1^{\mathrm{PNC}} - E_1^{\mathrm{PNC}*})}{|E_1^{\mathrm{PNC}}|^2 + |M_1|^2} \simeq -2\mathcal{R}, \quad (12)$$

where we used $|E_1^{\mathrm{PNC}}|^2 \ll |M_1|^2$ and $E_1^{\mathrm{PNC}*} = -E_1^{\mathrm{PNC}} = -i\,\mathrm{Im}(E_1^{\mathrm{PNC}})$ and introduced the factor $\mathcal{R}$:

$$\mathcal{R} \equiv \mathrm{Im}\left(\frac{E_1^{\mathrm{PNC}}}{M_1}\right). \quad (13)$$

Using Eqs. (1) and (12), the PNC optical-rotation angle is given by

$$\varphi_{\mathrm{PNC}} = -\frac{4\pi l}{\lambda}[n(\omega) - 1]\mathcal{R}, \quad (14)$$

where $n(\omega)$ is the index of refraction of the medium [Eqs. (7) and (12)], which is a function of the transition frequency ω. The proportionality relation between the PNC optical-rotation angle φ_{PNC} and the ratio $\mathcal{R}$ serves as the basis for this experimental technique.

Note that the corresponding electric dipole formulas for Eqs. (3), (2), and (8) are obtained simply by substituting $\mu_0 \to$

$1/\varepsilon_0$, where ε_0 is the vacuum permittivity, and $\langle M_1 \rangle \to \langle E_1 \rangle$. Here $\langle M_1 \rangle$ is given in units of μ_{B}, the Bohr magneton, and $\langle E_1 \rangle$ in units of $e\alpha_{\mathrm{B}}$, where α_{B} is the Bohr radius.

C. Nuclear-spin-dependent PNC effects: Anapole moment

Nuclear-spin-dependent (NSD) contributions to the atomic parity violation arise due to (a) neutral weak-current interactions between the electron and the nucleus [36], (b) electromagnetic interaction of the electron with the nuclear anapole moment [37], and (c) spin-independent electron-nucleon weak interactions combined with magnetic hyperfine interactions [38]. These contributions can be included in a dimensionless constant $\varkappa$, proportional to the strength of the NSD-PNC interaction [4,39,40]

$$\varkappa = \varkappa_A - \frac{\mathcal{K} - 1/2}{\mathcal{K}}\varkappa_2 + \frac{I+1}{\mathcal{K}}\varkappa_{Q_{\mathrm{W}}}, \quad (15)$$

where $\mathcal{K} = (-1)^{I+1/2-l}(I + 1/2)$ (l is the orbital angular momentum of the valence nucleon), $\varkappa_2 \approx -0.05$ [4,38] corresponds to the weak neutral currents, $|\varkappa_{Q_{\mathrm{W}}}| \approx 0.02$ [4] appears as a radiative correction to the nuclear-spin-independent (NSI) part, and $\varkappa_A$ is the nuclear anapole moment contribution to the NSD-PNC effects.

The nuclear anapole moment $\varkappa_A$ is given by (in a simple valence model) [39]

$$\varkappa_A = 1.15 \times 10^{-3} A^{2/3} \mu_m g_m, \quad (16)$$

where A is the number of nucleons and μ_m is the magnetic moment of the unpaired nucleon ($\mu_p = 2.8$ and $\mu_n = -1.9$). The dimensionless constant g_m gives the strength of the weak interactions between the nucleons. Theoretical estimates suggest that for neutrons $g_n \approx -1$ and for protons $g_p \approx 4.5$ [41]. From Eq. (16) we see that the nuclear anapole moment scales with the number of nucleons ($\varkappa_A \propto A^{2/3}$). For this reason, the anapole moment gives the largest contribution to NSD parity-violating effects in heavy atoms [4]. Using Eq. (16), we see that the value of the anapole moment is $\varkappa_A \approx 0.1$–1 [37,39].

The PNC matrix element is expressed in terms of a NSI and a NSD component as follows [4]:

$$\langle F \| E_1^{\mathrm{PNC}} \| F' \rangle = \langle F \| E_1^{\mathrm{PNC,(SI)}} \| F' \rangle + \langle F \| E_1^{\mathrm{PNC,(SD)}} \| F' \rangle$$
$$= K_{FF'} E_1^{\mathrm{PNC}}(1 + r_{FF'}\varkappa), \quad (17)$$

where $K_{FF'}$ is the angular factor [using $k = 1$ in Eq. (5)], $r_{FF'}$ is the ratio of spin-dependent to spin-independent PNC amplitudes, and $\varkappa$ is given by Eq. (15). From Eq. (17) we see that measuring the PNC amplitudes for two different hyperfine components of a specific transition allows the value of $\varkappa$ to be expressed by the ratio of the measured amplitudes.

The PNC rotation angle can be split into a NSI and a NSD part:

$$\varphi_{\mathrm{PNC}} = \varphi_{\mathrm{SD}} + \varphi_{\mathrm{SI}} = -\frac{4\pi l}{\lambda}[n(\omega) - 1](\mathcal{R}_{\mathrm{SI}} + \mathcal{R}_{\mathrm{SD}}). \quad (18)$$

Calculated values of E_1^{PNC}, $\mathcal{R}$, and the ratios $r_{FF'}$ (and thus $\mathcal{R}_{\mathrm{SI}}$ and $\mathcal{R}_{\mathrm{SD}}$) for the various proposed transitions in Xe, Hg, and I can be found in Refs. [23,34].

TABLE I. Reduced matrix elements for the M_1, E_1^{PNC}, and $\mathcal{R} \equiv \mathrm{Im}(E_1^{PNC})/M_1$ for the proposed atomic transitions. Note that for one absorption length $\varphi_{PNC}^{max} \approx \mathcal{R}/2$.

	Z	Transition	λ (nm)	M_1 (μ_B)	Isotopes with $I \neq 0$	$\mathrm{Im}(E_1^{PNC})$ $\times 10^{-10} e\alpha_B$	$\mathcal{R}$ $\times 10^{-8}$
I	53	$^2P_{3/2} \rightarrow {}^2P_{1/2}$	1315	1.15	^{127}I	0.335(67)	0.80(16)
		$^3P_0^o \rightarrow {}^1P_1^o$	609	0.229		3.4(2), 3.5(2)	41(2), 42(2)
Hg	80	$^3P_1^o \rightarrow {}^1P_1^o$	682	0.199	$\{^{199}\mathrm{Hg},^{201}\mathrm{Hg}\}$	5.3(3), 5.4(3)	73(4), 74(4)
		$^3P_2^o \rightarrow {}^1P_1^o$	997	0.272		3.7(2), 3.8(2)	37(2), 38(2)
Xe	54	$6s_2^{2[3/2]o} \rightarrow 6s_1^{'2[1/2]o}$	988	1.22	$\{^{129}\mathrm{Xe},^{131}\mathrm{Xe}\}$	3.17(31), 3.23(32)	7.1(7), 7.3(7)

III. ATOMIC SYSTEMS AND EXPERIMENTAL FEASIBILITY

A. Parity-nonconservation candidates: Xe, Hg, and I

We have identified the following favorable PNC transitions in the atomic systems of Xe, Hg, and I: (a) in metastable Xe, the $M1$ transition $(^2P_{3/2}^o)6s\,^2[3/2]_2^o \rightarrow (^2P_{1/2}^o)6s\,^2[1/2]_1^o$ with transition wavelength $\lambda = 988$ nm; (b) in metastable Hg, the transitions $6s6p\,^3P_J^o \rightarrow 6s6p\,^1P_1^o$ at 609 nm ($J = 0$), 682 nm ($J = 1$), and 997 nm ($J = 2$); and (c) the spin-orbit transition of ^{127}I, $^2P_{3/2} \rightarrow {}^2P_{1/2}$ with a transition wavelength of 1315 nm. Partial energy diagrams of the three proposed atomic systems are presented in Fig. 1.

In Bougas *et al.* [22], preliminary atomic calculations for the magnetic dipole $M1$ and the PNC electric dipole $E1_{PNC}$ transition amplitudes for the proposed transitions in metastable Xe and Hg were presented (note that the simulations presented in Ref. [22] were based on these preliminary calculations). More recently, Dzuba and Flambaum [34], using the configuration-interaction technique, presented calculations for the relevant transition dipole amplitudes of the proposed transitions in Xe and Hg. In particular, for the case of Hg, the spin-forbidden $M1$ transition amplitudes were overestimated in Ref. [22] and the calculated numbers for the $M1$ dipole amplitudes were found to be strongly suppressed. In the case of Xe the $M1$ dipole amplitude is found to be 6% different from the initial calculation presented in Ref. [22]. In this article we use the transition amplitudes presented in Ref. [34] for the simulations of the expected PNC optical-rotation signal under specific experimental conditions (see Sec. V). In Table I we summarize the results presented in Ref. [34], along with the preliminary atomic calculations for the dipole transition amplitudes of the proposed PNC optical-rotation scheme in ground-state I, as presented in Ref. [23].

B. Experimental feasibility

In the optical-rotation experiments using Tl, Bi, and Pb vapors, PNC optical-rotation angles of ~ 1 μrad were measured (in the case of Tl with an experimental precision of 1%) [11–13]. In order to achieve PNC rotation angles of the order of ~ 1 μrad, column densities of $\sim 10^{18}$–10^{19} cm^{-2} atoms were required (at temperatures of about ~ 1300 K), which correspond to optical depths of 10–60. Using Eq. (14), an estimate for the maximum expected PNC optical rotation signal can be given. Assuming a Lorentzian dispersion curve, Eq. (14) yields $\varphi_{PNC} \approx \mathcal{R}/2$ for one absorption length.

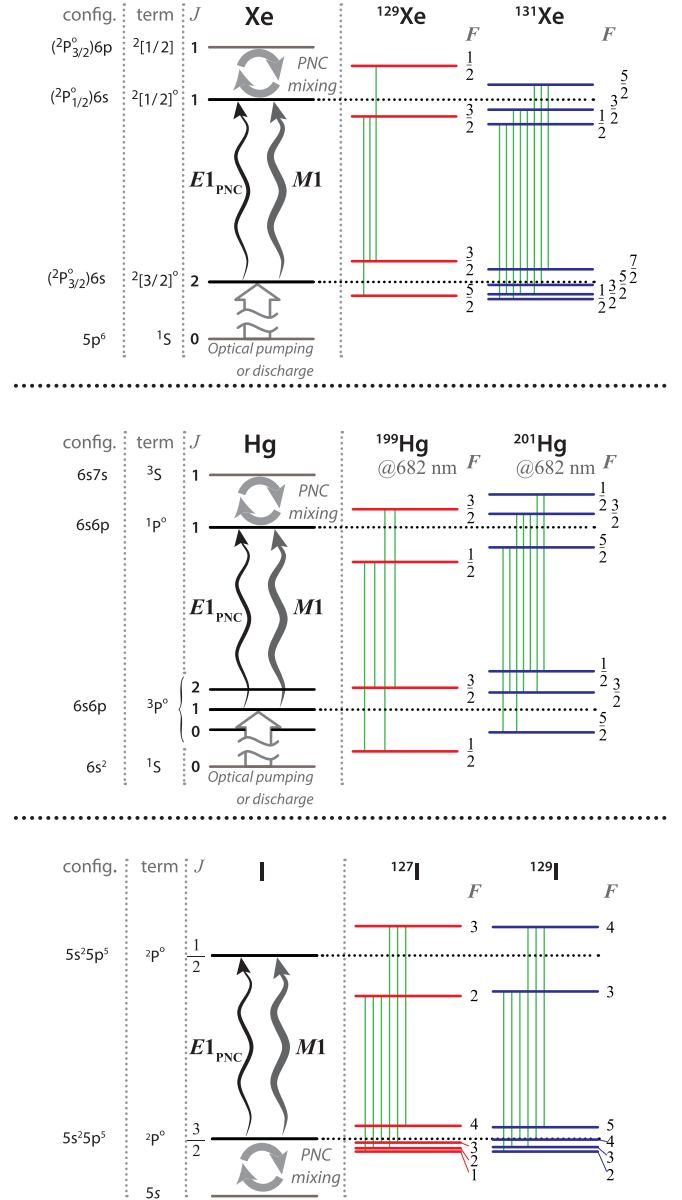FIG. 1. (Color online) Partial energy-level diagram of Xe, Hg, and I (not to scale) showing the proposed $E1_{PNC}$ and $M1$ transitions. In addition, the hyperfine-structure levels for the odd isotopes of Xe, Hg, and I are presented. For each atomic system, indicated in green, are the individual $F \rightarrow F'$ transitions constituting the separated hyperfine groups of Figs. 5–7. The values for the hyperfine-structure splittings and isotopic shifts for each of the proposed systems were taken from Refs. [42–47].

The production of Xe metastable states $6s\,^2[3/2]_2^o$ and Hg ^3P_J has been realized using low-pressure electrical discharge lamps [48,49] or optical pumping [50], yielding steady-state densities of about 10^{12} cm^{-3}, allowing column densities of about 10^{14} cm^{-2} (over a single-pass path length of 100 cm). Similarly, high iodine atom densities of $\sim 10^{16}$ cm^{-3} have been achieved in glow discharges (requiring high precursor and carrier gas pressures). Also, the photodissociation of I_2 molecules is expected to yield atomic densities of 10^{14}–10^{16} cm^{-3} of ground-state $^2P_{3/2}$ iodine atoms, obtaining thus single-pass column densities of 10^{16}–10^{18} cm^{-2} for an interaction path length of 100 cm [23].

Given the calculated values $\mathcal{R}$ for Xe, Hg, and I (Table I) and the experimentally feasible column densities for each of the proposed atomic systems stated above, we see that single-pass PNC optical-rotation angles of $\sim 10^{-11}$–10^{-9} rad are expected. The polarization rotation noise per unit bandwidth in a balanced polarimeter is ~ 2 nrad/$\sqrt{\text{Hz}}$ (assuming shot-noise-limited detection for a probe beam with an intensity of ~ 10 mW). This reasoning dictates that an additional enhancement factor ($\sim 10^2$–10^4) is necessary to achieve measurable signals.

In the following section we revisit the experimental technique proposed in Ref. [22] and describe in detail the principles of the cavity-enhanced scheme as well as the measurement procedure.

IV. CAVITY-ENHANCED POLARIMETRY

In comparison to a single-pass instrument, a cavity-enhanced polarimeter introduces a phase-shift enhancement factor of $2\mathcal{F}/\pi$, where $\mathcal{F} \equiv \pi\sqrt[4]{R_t}/(1-\sqrt{R_t})$ is the finesse of the cavity ($R_t = R_1R_2R_3R_4$, where R_i is the reflectivity of the ith mirror). Using high-finesse cavities, measurements with shot-noise-limited phase-shift resolution at the level of 3×10^{-13} rad have been demonstrated [51].

In Ref. [22], a cavity-enhanced polarimetric technique implementing signal reversals was proposed for the enhancement and precise measurement of the PNC optical-rotation angle φ_{PNC} (14). The experimental scheme consists of a four-mirror cavity in a bow-tie configuration. A four-mirror cavity design has three main advantages over linear cavities: (a) It provides the ability of measuring simultaneously polarization effects of different symmetry under time reversal (as in the case of magneto-optical effects and natural optical activity) without altering the apparatus during measurements, (b) it supports counterpropagating beams, which give an immediate signal reversal, and (c) it avoids mechanical adjustments of possible intracavity optical elements, as in the case of two-mirror cavities used for the measurement of natural optical activity in the gas phase where intracavity quarter-wave plates needed to be modulated mechanically [52]. In this section we present the eigenpolarization theory for the cavity-enhanced polarimeter, based on the Jones matrix calculus [53–55] and discuss in detail the principles of the proposed experimental technique.

In the Jones matrix formalism, the effect of any optical element on the polarization state vector of the laser light is described as a linear operator, expressed by a 2×2 matrix whose matrix elements are in general complex. The direct incorporation of amplitude and phase information allows

for the investigation of coherent phenomena. Furthermore, since the incident clockwise and counterclockwise beams will be mode matched into the TEM$_{00}$ mode of the four-mirror cavity, we focus our analysis on the polarization properties of the longitudinal modes for either propagation direction. In addition, changes in the spatial profile of the laser beams, introduced by the intracavity elements, are neglected. The Jones matrices corresponding to each of the optical elements used in the proposed apparatus are denoted hereafter by boldface letters $\mathbf{J}$.

A. Jones matrices for polarization optics

The Jones matrix for reflection is the same for clockwise and counterclockwise propagation and is given by

$$\mathbf{J}_{M_i}(\delta_i) = \sqrt{R_i}\begin{pmatrix} -e^{i\delta_i/2} & 0 \\ 0 & e^{-i\delta_i/2} \end{pmatrix}, \qquad (19)$$

where the index i ranges from 1 to 4. We assume that the Fresnel amplitude reflection coefficients for the s and p polarizations are equal in magnitude (an assumption expressed by the common factor $\sqrt{R_i}$), which is a good approximation for near-normal angle-of-incidence reflections, as in the case of a bow-tie cavity. The differential s-p phase shift $\delta_i = \delta_p - \delta_s$ represents the linear birefringence obtained upon mirror reflection. For non-normal incidence, these s-p phase shifts can be of the order of 10^{-3} rad, while for normal incidence they are of the order of 10^{-5}–10^{-6} rad at a specific design wavelength (for gyroquality supermirrors at normal incidence, the linear birefringences can be as low as ~ 0.1 μrad) [56].

In the presence of a longitudinal magnetic field a medium becomes circular birefringent, an effect otherwise know as the Faraday effect [57]. The Faraday optical rotation is expressed as $\theta_F = VBl$, where B is the magnetic-field strength along the direction of light propagation, l is the path length of interaction, and V is the Verdet constant of the medium. The Jones matrix for the Faraday rotation is an SU(2) rotation matrix with argument θ_F:

$$\mathbf{J}_F(\theta_F) = \begin{pmatrix} \cos\theta_F & -\sin\theta_F \\ \sin\theta_F & \cos\theta_F \end{pmatrix}. \qquad (20)$$

Note that the physical direction of the polarization rotation is defined by the magnetic-field orientation. Due to the nonreciprocal nature of the Faraday effect, when either the magnetic field or the direction of propagation of the light reverses, the sign of rotation reverses (in the light frame). Thus, for the counterclockwise propagation, the Faraday rotation will be $\theta_F^{\text{CCW}} \rightarrow -\theta_F^{\text{CW}}$. As we shall see, this directional symmetry breaking, induced by the Faraday effect, is essential to our signal reversals.

The Jones matrix representing the PNC optical rotation will also be that of an SU(2) rotation matrix with argument φ_{PNC}:

$$\mathbf{J}_{\text{PNC}}(\varphi_{\text{PNC}}) = \begin{pmatrix} \cos\varphi_{\text{PNC}} & -\sin\varphi_{\text{PNC}} \\ \sin\varphi_{\text{PNC}} & \cos\varphi_{\text{PNC}} \end{pmatrix}, \qquad (21)$$

where φ_{PNC} is given by Eq. (14). The PNC optical rotation, being a pseudoscalar quantity, is odd under parity transformations *and* even under time-reversal transformations. Therefore, the Jones matrix describing PNC optical rotation will be the

same for both clockwise and counterclockwise propagation directions $\varphi_{PNC}^{CW} = \varphi_{PNC}^{CCW}$.

Finally, anisotropies such as imperfections of transmission optics, thermal- or stress-induced birefringences, and stray magnetic fields can be described as linear birefringent optical elements. The Jones matrix for a general linear wave retarder, which introduces a differential phase shift δ' and whose "fast axis" is oriented at an angle θ with respect to the x axis, is given by

$$\mathbf{J}(\theta, \delta') = S(\theta) \times \begin{pmatrix} e^{i\delta'/2} & 0 \\ 0 & e^{-i\delta'/2} \end{pmatrix} \times S(-\theta), \quad (22)$$

where $S(\theta)$ describes a general SU(2) rotation matrix. Reversing the direction of propagation (in the light frame) reverses the sign of the angle θ, which specifies the orientation of the retardation axes. For the mirror-reflection linear birefringence, we used $\mathbf{J}(\theta, \delta')$ for $\theta = 0$. Note that the eigenvectors of the $\mathbf{J}(\theta, \delta')$ are linear polarization states.

B. Clockwise and counterclockwise round-trip matrices

The round-trip Jones matrices for the clockwise (counterclockwise) propagation are obtained by the ordered multiplication of the Jones matrices representing the optical elements. A convenient starting point for the analysis is the point labeled O in Fig. 2, from which the different propagation directions are defined. The round-trip Jones matrices are given by

$$\mathbf{J}^{CW} = \mathbf{J}_{M_2}(\delta/4) \cdot \mathbf{J}_{M_3}(\delta/4) \cdot \mathbf{J}(\varphi_{PNC}) \cdot \mathbf{J}(\theta_F)$$
$$\cdot \mathbf{J}_{M_4}(\delta/4) \cdot \mathbf{J}_{M_1}(\delta/4) \quad (23)$$

for the clockwise propagation path and

$$\mathbf{J}^{CCW} = \mathbf{J}_{M_2}(\delta/4) \cdot \mathbf{J}_{M_3}(\delta/4) \cdot \mathbf{J}(-\theta_F) \cdot \mathbf{J}(\varphi_{PNC})$$
$$\cdot \mathbf{J}_{M_4}(\delta/4) \cdot \mathbf{J}_{M_1}(\delta/4) \quad (24)$$

for the counterclockwise propagation path. Here we define δ as the total single-pass linear birefringence. Note that reversing the order of the individual operators and changing the sign of each Faraday rotation angle for the clockwise (counterclockwise) path produces the counterclockwise (clockwise) path (if an additional linear birefringent element is present, then the sign of its respective orientation angle should be also reversed so as to obtain the counterclockwise propagation matrix).

The Jones matrices for the Faraday rotation and the PNC rotation are commutable, a property that reflects the fact that rotations about the same axis are additive [$\mathbf{J}(\varphi_{PNC}) \cdot \mathbf{J}(\theta_F) = \mathbf{J}(\varphi_{PNC} + \theta_F)$]. Therefore, the total single-pass optical rotation is different for the clockwise and counterclockwise counterpropagating beams

$$\alpha_{CW} = \theta_F + \varphi_{PNC}, \quad \alpha_{CCW} = -\theta_F + \varphi_{PNC}. \quad (25)$$

This directional symmetry breaking is key for distinguishing the PNC and Faraday-type optical rotation and thus for the sensitive measurement of the PNC optical-rotation angle.

Rewriting Eqs. (23) and (24) in a compact form, we have

$$\mathbf{J}^{CW} = R^2 \cdot \mathbf{J}(0, \delta/2) \cdot \mathbf{J}(\alpha_{CW}) \cdot \mathbf{J}(0, \delta/2), \quad (26)$$

$$\mathbf{J}^{CCW} = R^2 \cdot \mathbf{J}(0, \delta/2) \cdot \mathbf{J}(\alpha_{CCW}) \cdot \mathbf{J}(0, \delta/2), \quad (27)$$
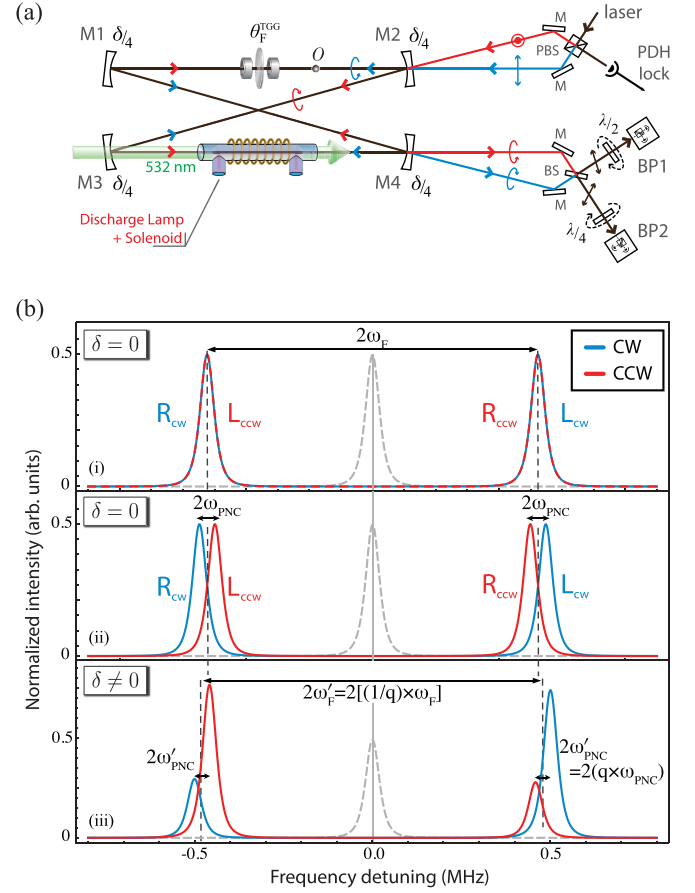
(a)

(b)

FIG. 2. (Color online) (a) Proposed experimental setup. The input laser beam is split into two parts of equal intensity and orthogonal polarizations. The laser frequency is brought into resonance with the nearly degenerate R_{CW}-L_{CCW} modes of the cavity. Upon exit from the cavity, the counterpropagating outputs are recombined into linearly polarized light and analyzed with linear and circular balanced polarimeters (BP1 and BP2, respectively). The 532-nm laser beam that will be used for the production of high atomic iodine densities through the photodissociation of I_2 is also depicted. (b) Cavity frequency polarization spectrum. For the simulations we used $\theta_F = 13$ mrad and $\delta = \theta_F/2 = 6.5$ mrad and for demonstration purposes $\varphi_{PNC} = 0.6$ mrad. (i) The Faraday effect splits the cavity spectrum into R and L modes by $2\omega_F = 2\theta_F(c/L)$ (twofold degeneracy); (ii) the PNC optical rotation splits further the clockwise (CW) and counterclockwise (CCW) modes by $2\omega_{PNC} = 2\varphi_{PNC}(c/L)$, while the cavity modes remain circular polarization states; (iii) in the presence of linear birefringence ($\delta \neq 0$) the frequency splitting of the eigenmodes increases as $\omega_F' = 1/q\omega_F$ and the measured PNC-induced splitting is reduced $\omega_F' = q\omega_F$ ($0 \leq q \leq 1$) (see Fig. 3); the eigenmodes transform into elliptical states as observed from the different amplitudes of the output light (see the text for discussion). We also assume that the clockwise input beam was p polarized, while the counterclockwise beam was s polarized. The cavity's linewidth is exaggerated for demonstration purposes; note that the free spectral range of the cavity is $\Delta\omega_{FSR} = 2\pi \times 40$ MHz. In (i)–(iii), the gray dashed line corresponds to the fourfold degenerate axial mode of an isotropic cavity. PBS stands for polarizing beam splitter and BS stands for beam splitter.

where we omit the mirror index under the assumption that all four mirrors have the same reflectivity and linear birefringence.

C. Frequencies and polarizations of the cavity spectrum

The allowed polarizations of the cavity modes, along with their respective frequencies, are determined by the anisotropies of the cavity. Using the explicit form of the transfer matrices for clockwise and counterclockwise propagation [Eqs. (26) and (27)], we can obtain the eigensystem for both directions as a function of the anisotropy parameters (θ_F, φ_{PNC}, and δ) [55]. For the following discussion, we set $R = 1$, as we are interested only in the properties of the frequency spectrum of the optical resonator.

The matrices $\mathbf{J}^{CW}$ and $\mathbf{J}^{CCW}$ are unitary matrices of rank 2. Therefore, each matrix has two eigenvalues and two eigenvectors; the eigenvectors $v_\pm$ are generally complex, orthogonal vectors and represent the eigenpolarizations of each cavity mode. The eigenvalues can be written in the form $\lambda_\pm = e^{\pm i\Phi}$. The phase of each eigenvalue is the round-trip optical phase shift obtained during light propagation and therefore yields the frequency splittings of the eigenmodes.

In the simple case of an isotropic cavity ($\alpha = 0$ and $\delta = 0$), the four eigenmodes are degenerate and any polarization state can couple into the cavity ($\mathbf{J}^{CW}$ and $\mathbf{J}^{CCW}$ become proportional to the identity matrix for $\alpha = 0$ and $\delta = 0$). The introduction of anisotropies lifts this fourfold degeneracy. Therefore, in the most general case, the spectrum of the cavity is represented by four nondegenerate modes of elliptical polarization, whose frequencies lie above and below the degenerate frequency of the isotropic case. We examine three cases.

(i) $\theta_F \neq 0$, $\varphi_{PNC} = 0$, and $\delta = 0$. The Jones matrices for clockwise and counterclockwise become

$$\mathbf{J}^{CW} = \mathbf{J}_F(\theta_F), \quad \mathbf{J}^{CCW} = \mathbf{J}_F(-\theta_F). \tag{28}$$

It is easy to verify that the allowed eigenpolarizations of a rotation matrix are circular polarization states. Therefore, in the presence of single-pass Faraday rotation θ_F, the spectrum splits into right-circular and left-circular polarization modes; the frequency splitting is equal to $2\omega_F = 2\theta_F(c/L)$, where c is the speed of light and L is the round-trip cavity length. The nonreciprocal nature of the Faraday effect, embedded in the change of sign of the Faraday rotation when the direction of propagation is reversed, is directly reflected in the frequency spectrum of the cavity. The R_{CW} mode is degenerate with the L_{CCW}, while the R_{CCW} mode is degenerate with the L_{CW} mode [see Fig. 2(b), case (i)].

(ii) θ_F, $\varphi_{PNC} \neq 0$, and $\delta = 0$. For single-pass rotations φ_{PNC} and θ_F and in the absence of any linear birefringence ($\delta = 0$), the round-trip matrices for clockwise and counterclockwise correspond to rotation matrices with arguments α_{CW} and α_{CCW} [Eq. (25)]:

$$\mathbf{J}^{CW} = \mathbf{J}(\alpha_{CW}), \quad \mathbf{J}^{CCW} = \mathbf{J}(\alpha_{CCW}). \tag{29}$$

The eigenpolarizations remain circular polarization states for both propagation directions since the transfer matrices are simply rotation matrices. Their respective eigenvalues are $\lambda_{CW}^\pm = e^{\pm i\alpha_{CW}}$ and $\lambda_{CCW}^\pm = e^{\pm i\alpha_{CCW}}$. The difference in rotation [Eq. (25)] results in splitting the clockwise and counterclockwise modes by $2\omega_{PNC} = 2\varphi_{PNC}(c/L)$, yielding the four-mode structure depicted in Fig. 2(b), case (ii).

(iii) θ_F, φ_{PNC}, and $\delta \neq 0$. Linear birefringence prevents the enhancement of circular birefringence through the transformation of a linearly polarized beam into a circular one. If, however, a large circular birefringence is induced, then the effects of linear birefringence will be averaged out [22,54]. Using the general form of the clockwise and counterclockwise matrices [Eqs. (26) and (27)], we demonstrate how the extraction of φ_{PNC} is affected in the presence of δ. Expanding Eqs. (26) and (27), we obtain

$$\mathbf{J}^{CW} = \begin{pmatrix} e^{i\delta/2}\cos(\theta_F + \varphi_{PNC}) & -\sin(\theta_F + \varphi_{PNC}) \\ \sin(\theta_F + \varphi_{PNC}) & e^{-i\delta/2}\cos(\theta_F + \varphi_{PNC}) \end{pmatrix}, \tag{30}$$

$$\mathbf{J}^{CCW} = \begin{pmatrix} e^{i\delta/2}\cos(\theta_F - \varphi_{PNC}) & \sin(\theta_F - \varphi_{PNC}) \\ -\sin(\theta_F - \varphi_{PNC}) & e^{-i\delta/2}\cos(\theta_F - \varphi_{PNC}) \end{pmatrix}. \tag{31}$$

The eigenvalues and eigenvectors are

$$\lambda_{CW}^\pm = \cos\alpha_{CW}\cos\frac{\delta}{2} \mp i\sqrt{1 - \cos^2\alpha_{CW}\cos^2\frac{\delta}{2}},$$
$$v_{CW}^\pm \propto \begin{pmatrix} \csc\alpha_{CW}\left(\cos\alpha_{CW}\sin\frac{\delta}{2} \mp \sqrt{1 - \cos^2\alpha_{CW}\cos^2\frac{\delta}{2}}\right) \\ -i \end{pmatrix} \tag{32}$$

for the clockwise transfer matrix and

$$\lambda_{CCW}^\pm = \cos\alpha_{CCW}\cos\frac{\delta}{2} \mp i\sqrt{1 - \cos^2\alpha_{CCW}\cos^2\frac{\delta}{2}},$$
$$v_{CCW}^\pm \propto \begin{pmatrix} \csc\alpha_{CCW}\left(\cos\alpha_{CCW}\sin\frac{\delta}{2} \mp \sqrt{1 - \cos^2\alpha_{CCW}\cos^2\frac{\delta}{2}}\right) \\ i \end{pmatrix} \tag{33}$$

for the counterclockwise transfer matrix. We see that in the most general case the polarization eigenstates for both the clockwise and counterclockwise modes are represented by orthogonal ellipses and their frequency splitting is proportional to $\Gamma = \cos^{-1}[\cos\alpha\cos(\frac{\delta}{2})]$.

Linear birefringence δ prevents the effective amplification of circular birefringence α by transforming the cavity modes into elliptical polarization states. Therefore, the measurement of φ_{PNC} in the presence of linear birefringence will be reduced to $\varphi'_{PNC} = q\varphi_{PNC}$, where q ($0 \leq q \leq 1$) is the reduction factor.
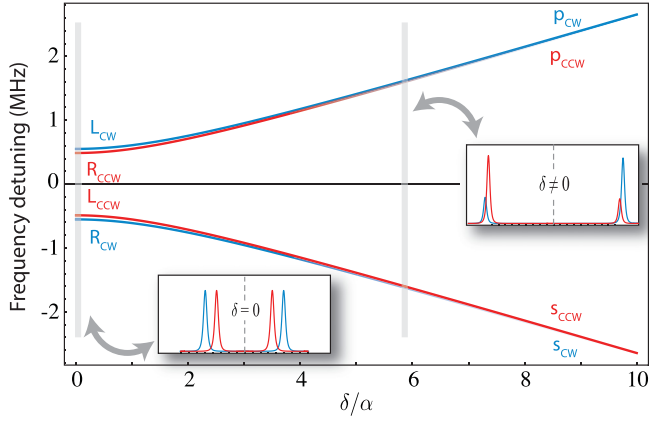
FIG. 3. (Color online) The presence of linear birefringence δ prevents the enhancement of the PNC optical rotation φ_{PNC}. The resonance peaks of the cavity eigenpolarization frequency spectrum are presented as a function of the ratio δ/α. As δ increases, and therefore the magnitude of the total cavity anisotropies increases, the frequency difference between the respective clockwise (or counterclockwise) R-L modes increases by $1/q$, while the PNC-induced frequency splitting (exaggerated here for clarity) decreases by q [Eq. (34)]. For the simulations we used $\theta_F = 13$ mrad and $\varphi_{\text{PNC}} = 0.8$ mrad (this value of φ_{PNC} was chosen purely for demonstration purposes).

From Eq. (32) and (33) we obtain the form of the reduction factor for $\varphi_{\text{PNC}} \ll 1$:

$$q = \frac{\Gamma - \Gamma|_{\varphi_{\text{PNC}}=0}}{\varphi_{\text{PNC}}} = \frac{\cos\frac{\delta}{2}\sin\theta_F}{\sqrt{1 - \cos^2\frac{\delta}{2}\cos^2\theta_F}} + \mathcal{O}(\varphi_{\text{PNC}}).$$

(34)

In Fig. 3 we investigate the effect of the linear birefringence δ as a function of the ratio of the total linear birefringence anisotropy over the total circular birefringence δ/α. The introduction of this extra anisotropy δ will increase the frequency splitting of the modes for each sense of propagation. This effective increase in frequency is inversely proportional to and equal in magnitude to the simultaneous decrease of the PNC-induced splitting, i.e., $2\Gamma/(2\Gamma|_{\delta=0}) \equiv 1/q$ (Fig. 3). Figure 2(b), case (iii) and Fig. 3 show simulations based on Eqs. (32) and (33), which demonstrate how the presence of linear birefringence prohibits the enhancement of circular birefringence, as the PNC-induced mode splitting vanishes for large δ/α. Note that the cavity's eigenpolarization modes become more elliptical with increasing δ; the input beams are linearly polarized and therefore the induced ellipticity is depicted on the different intensity amplitudes of the cavity (output) modes. Therefore, to ensure $q \cong 1$, one must satisfy $\alpha \gg \delta$ (see also the relevant discussion in Ref. [22]).

For the numerical simulations presented in Figs. 2(b) and 3, we assumed that each mirror introduces a linear birefringence phase shift equal to $\delta/4$ and that the optical axes of all four cavity mirrors are parallel. As discussed previously, the important parameter is the total introduced linear birefringence and in the case where the optical axes of the mirrors are parallel, then the mirror-related linear birefringent phase shifts will add. In contrast, for random orientations of the mirrors optical

axes, there will be partial cancellation of the total introduced birefringence. Thus, the reduction factor presented in Fig. 3 represents the worst-case estimation.

D. Principles of the measurement

The principles of the measurement have been described previously in Ref. [22] and are briefly discussed here. We will assume for the following discussion a bow-tie four-mirror cavity with round-trip cavity length $L = 7.5$ m.

A laser beam is split into two beams of equal intensity and orthogonal linear polarizations. The s-polarized laser beam is locked to the R_{CW} mode and frequency-locked using the Pound-Drever-Hall (PDH) scheme [58]. Note that alternative locking schemes have also demonstrated shot-noise-limited phase-shift measurements (see Ref. [51] and references therein). The PNC-related mode splitting is equal to $2\omega_{\text{PNC}} = 2\varphi_{\text{PNC}}c/L$. For the different values of $\mathcal{R}$ presented in Table I, we obtain $\omega_{\text{PNC}}^{\max} \sim 150$ mHz to 15 Hz. The PNC-induced mode splitting is much smaller than the cavity linewidth $\Delta\omega_{\text{cav}}$ (for $L = 7.5$ m and $\mathcal{F} \sim 1.5 \times 10^4$, $\Delta\omega_{\text{cav}} = 2\pi \times 2.5$ kHz). Therefore, the p-polarized laser beam excites the nearly degenerate L_{CCW} mode [see Fig. 2 (b)]. The spatial recombination of the R_{CW} and L_{CCW} output beams produces a linearly polarized beam rotated by $N\varphi_{\text{PNC}}$, where N is the average number of round-trip cavity passes. The rotation angle $N\varphi_{\text{PNC}}$ will be measured with a balanced polarimeter. Note that the spatial recombination of the two output beams is expected to be a source of depolarization, for which the signal needs to be corrected. Therefore, we propose the use of two separate balanced polarimeters, implementing rotating half-wave and quarter-wave plates, respectively, yielding the complete set of Stokes parameters of the output recombined light (see Ref. [59]).

Observe that by bringing the clockwise and counterclockwise beams into resonance with the R_{CCW}-L_{CW} mode pair, the recombination of the exit beams will give now a signal output of $-N\varphi_{\text{PNC}}$, yielding thus a net difference in polarization rotation of $2N\varphi_{\text{PNC}}$. This is accomplished through the use of two signal reversals. First, the frequency of the laser can be brought into resonance with the R_{CCW}-L_{CW} mode pair with the use of an acoustic optic modulator. Second, reversing the magnetic field is equivalent to the interchange of the clockwise and counterclockwise beams and thus the laser will couple to the R_{CCW}-L_{CW} mode pair. These two signal reversals allow for the absolute measurement of the PNC optical rotation, avoiding the need for cell removal, as was required in previous PNC optical-rotation experiments. Additionally, these reversals can be performed at high frequencies of ~ 1 kHz, allowing a sufficient subtraction of experimental drifts. Note that the frequency of the reversals are constrained by the photon lifetime inside the cavity [for $R = R_1 R_2 R_3 R_4 = 0.9999^4$ then $\tau_{\text{photon}} = L/(c|\ln R|) \sim 63$ μs].

In the previous sections we saw that a linear birefringence can suppress the enhancement of the PNC optical rotation. In general, linear birefringences originating from mirror-reflection phase shifts and thermal and/or stress-induced birefringences are expected to be $\sim 10^{-3}$ rad (per single pass per reflection or transmission). Inducing a large circular birefringence protects the coherent accumulation of the PNC

optical rotation inside the cavity. The circular birefringence can be induced using the Faraday effect of the proposed transitions themselves. Theoretical calculations for the Faraday effect on the $M1$ transitions under consideration and the proposed column densities yield $\theta_F \sim 10^{-3}$ rad for a 200-G magnetic field [25,26]. An alternative is the use of an antireflection-coated high-Verdet-constant glass window inside the cavity, a dense flint glass for example. A terbium gallium garnet (TGG) crystal has a Verdet constant of $V \sim 45$ μrad G^{-1} cm^{-1} with losses of $\sim 10^{-4}$/mm^{-1} at 1064 nm. For a 1-mm crystal thickness and magnetic fields of 3000 G one obtains $\theta_F \sim 13.5$ mrad, ensuring that $\alpha \gtrsim 10\delta$, for which the depolarization factor $q \gtrsim 0.9993$ (see also discussion in Ref. [22]). Finally note that in the case of large linear birefringences, a compensator (for example, a thin MgF$_2$ glass) with antireflection coatings can be placed appropriately to reduce the cavity's total linear birefringence and therefore to satisfy the condition $\alpha \gtrsim 10\delta$.

As a final remark, note that the metastable Xe and Hg are produced in a discharge lamp or via optical pumping, or in the case of I from molecular photodissociation, and can thus be switched on and off. This gives us an additional subtraction procedure that allows for the real-time investigation of the "empty" cavity and thus of possible experimental errors.

V. THEORETICAL SIMULATIONS

A. Optical absorption length

Upon exiting from the cavity, the recombined laser beams will be analyzed by a balanced polarimeter. The signal S is given by

$$S = 2N\varphi_{\text{PNC}}(\omega)T(\omega), \tag{35}$$

where N is the average number of round-trip cavity passes, $\varphi_{\text{PNC}}(\omega)$ denotes the dispersive line shape of the PNC optical rotation, and $T(\omega)$ is the transmission of the light beam through the vapor, which is governed by the Beer-Lambert law [27]

$$T(\omega) = \frac{I(\omega)}{I_0} = e^{-A(\omega)} \equiv e^{-\rho\sigma(\omega)l}. \tag{36}$$

Here $A(\omega)$ is the absorptivity, l is the interaction path length, ρ is the number density of the atoms, $\sigma(\omega)$ is the absorption cross section, which is a function of the optical frequency, and I_0 is the intensity of the incident laser beam.

The absorption cross section σ is given by the expression

$$\sigma(\omega) = \sigma_0 \sum_i \sum_{F,F'} b_i C_{FF'} \mathcal{V}''_{FF',i}(\omega), \tag{37}$$

where b_i is the abundance of isotope i (see Appendix B), the $C_{FF'}$ are geometrical factors [Eq. (B6)], and $\mathcal{V}''_{FF'}$ is the absorptive part of the Voigt profile [given in Eq. (A5)]. In the equation above, the integrated absorption cross section σ_0 is

$$\sigma_0 = \frac{\pi\mu_0\omega_{JJ'}}{\hbar c} \frac{1}{2J+1} \frac{M_1^2}{3}. \tag{38}$$

Note that $\sum_i \sum_{F,F'} b_i C_{FF'} = 1$ and, since $\int_0^\infty \mathcal{V}''(\omega)d\omega = 1$, we obtain $\int_0^\infty \sigma(\omega)d\omega = \sigma_0$, hence σ_0 is justifying its name. In addition, note that σ_0 has units of (area)×(angular frequency).

The extremely long effective path lengths, which can be realized in stable high-finesse optical cavities, lead to large
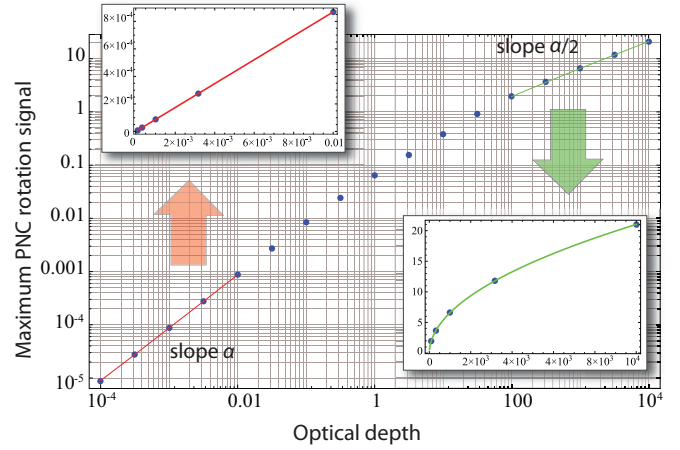

FIG. 4. (Color online) The PNC optical-rotation signal is proportional to the product $\varphi_{\text{PNC}}(\omega)T(\omega)$ [Eq. (35)]. Assuming Voigt line-shape profiles, the maximum PNC rotation signal is plotted as a function of the resonant optical depth (OD). We demonstrate that the signal scales linearly with OD when the vapor is optically thin and continues to increase with a square-root dependence as the vapor becomes thicker. The y axis is given in units of μrad and we assumed $\mathcal{R} = 14 \times 10^{-8}$.

effective resonant absorption lengths. In Fig. 4 we present calculations for the maximum PNC optical-rotation signal expected, as a function of the resonant absorption optical lengths l_0. The PNC optical-rotation signal is proportional to the product $\varphi_{\text{PNC}}(\omega)T(\omega)$ [Eq. (35)], i.e., proportional to the product of a dispersive line-shape profile times an absorption line-shape profile. For resonant optical depths $l_0 \ll 1$, the maximum PNC optical-rotation angle increases linearly with increasing column densities, i.e., $\varphi_{\text{PNC}}^{\text{max}} \propto \rho l$ (where ρ is the density and ρl is column density of the vapor), as shown in the upper inset of Fig. 4. For optical depths $l_0 \gg 1$, the vapor is optically thick near the line center where φ_{PNC} is largest and can no longer be observed. The effective maximal rotation angle is shifted further off resonance as $\sqrt{\rho l}$ and $\varphi_{\text{PNC}}^{\text{max}} \propto \sqrt{\rho l}$, as can be shown by maximizing the product of dispersion and transmission. Therefore, the rotation angle can still be increased with increasing column density for $l_0 \gg 1$, albeit with a rate slower than linear (see the lower inset of Fig. 4).

Finally, note that the average number of cavity passes N (which is a measure of the effective path length) needs to be determined precisely so that φ_{PNC} can be determined from the experimental observable $N\varphi_{\text{PNC}}$ [Eq. (35)]. Such measurements will be needed particularly near absorption lines where (for large resonant optical depths) N will be reduced and wavelength dependent. A well-established method for measuring N is the cavity ring-down technique [60].

B. Parity-nonconserving optical-rotation simulations

In this section we present theoretical simulations of the PNC optical-rotation signals for the proposed transitions in Xe, Hg, and I, where we explore a range of experimentally feasible parameters. We assume a four-mirror bow-tie cavity of round-trip cavity length $L = 7.5$ m (free spectral range $\Delta\omega_{\text{FSR}} = 2\pi \times 40$ MHz), each mirror having a reflectivity
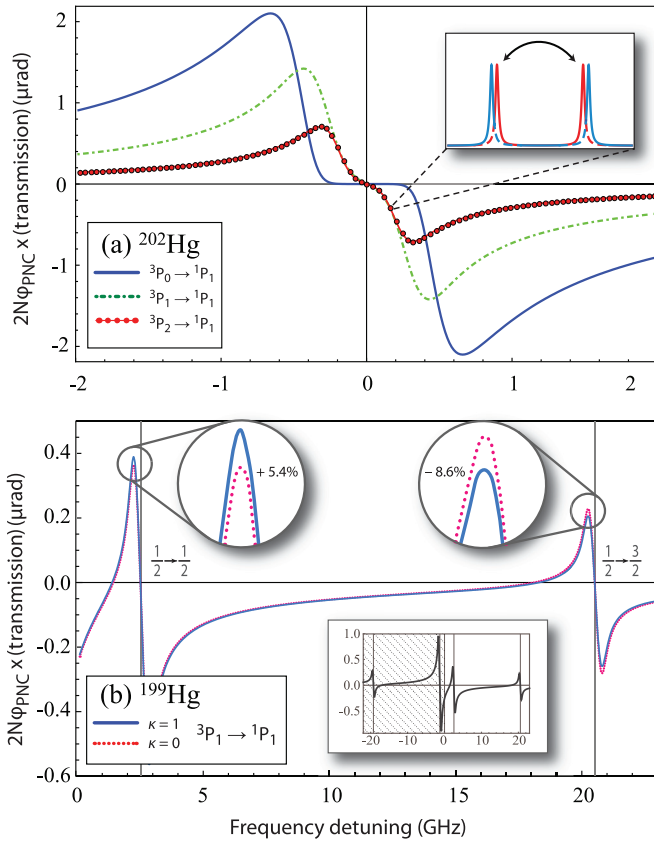
FIG. 5. (Color online) Theoretical simulations of the PNC optical-rotation signal in Hg vs optical frequency for two cases. (a) Simulations for the three proposed transitions (transition wavelength λ = 609, 682, and 997 nm) assuming a discharge lamp filled with isotopically pure ^{202}Hg, which produces for all the initial states $^3P_0$, $^3P_1$, and $^3P_2$ densities of $\rho = 5 \times 10^{12}$ cm^{-3}. In addition, identical Lorentz line widths $\Gamma_L = 2\pi \times 100$ MHz for all transitions are used, while the Doppler line widths for the 609-, 682-, and 997-nm transitions are $\sim 2\pi \times 183$, 163, and 112 MHz, respectively. The (red) points in the $^3P_2 \rightarrow {}^1P_1$ transition are separated by one FSR ($2\pi \times 40$ MHz) and the inset shows the reversal mechanism, which allows for the switching between different polarization mode pairs yielding thus a net polarization difference of $2N\varphi_{PNC}$. (b) We assume a discharge lamp filled with isotopically pure odd-isotope ^{199}Hg producing densities of $\rho = 5 \times 10^{12}$ cm^{-3} and a transitional Lorentz contribution of $\Gamma_L = 2\pi \times 100$ MHz. The inset shows the full hyperfine structure of the transition (the hyperfine-structure values were taken from Refs. [42,43]). The effect of the nuclear anapole moment is presented, setting $\varkappa = 1$ to yield visibly large signal differences. See the text for a detailed discussion. All values were taken from Ref. [34].

of $R = 99.99\%$ (enhancement factor $N \sim 10^4$) and a gas-cell (lamp) path length of $l = 1.5$ m. We present the enhanced PNC optical rotation $2N\varphi_{PNC}(\omega)$ multiplied by the transmission, which depends on the absorptivity of the specified transition through the atomic medium (Sec. V A).

1. Hg

In Fig. 5 we present the theoretical PNC optical-rotation simulations for the proposed transitions in Hg (using the

values for $\mathcal{R}$ from Ref. [34] as presented in Table I). In Fig. 5(a) we assume equal densities $\rho = 5 \times 10^{12}$ cm^{-3} of pure ^{202}Hg for all the initial states of the proposed PNC transitions ($^3P_0$, $^3P_1$, and $^3P_2$), produced in a discharge lamp (or using an optical pumping scheme). The line shape is a Voigt profile, with a Doppler contribution in the line width of $\Gamma_D \simeq 2\pi \times 267$, 238, and 163 MHz for the 609-, 682-, and 997-nm transitions, respectively [see Eq. (A4) for ~ 320 K]. The Lorentzian contribution for all three lines was taken to be $\Gamma_L = 2\pi \times 100$ MHz. This assumption is based on the fact that in a low-pressure discharge lamp (< 10 mTorr), the pressure broadening mechanisms are negligible compared to other homogeneous broadening mechanisms [48]. Therefore, the main contributions come from radiative processes. Lines originating from the ^3P_J states have Lorentz linewidths on the order of 20 MHz and for lines originating from the $^1P_1$ state on the order of 100 MHz [48]. Assuming an effective path length of 150×10^4 cm, we get column densities that correspond to 12, 3, and 3 absorption lengths at the strongest resonance for the 609-, 682-, and 997-nm transitions, respectively.

In Fig. 5(b) we examine the nuclear-spin-dependent PNC effects for the 682-nm transition in ^{199}Hg (nuclear spin $I = 1/2$). Using the values calculated by Dzuba and Flambaum in Ref. [34] for the PNC amplitudes between different hyperfine components and by setting $\varkappa = 1$, we see that the peak signals differ by about 5.4% and -8.6%, resulting in total signal differences of up to $\sim 14\%$. The actual value of $\varkappa$ can be estimated using Eqs. (15) and (16) to be ~ 0.1 for the Hg nucleus. Therefore, achieving an experimental precision of at least 0.25% is necessary to measure the NSD-PNC effects with a 6σ precision in the 682-nm transition for ^{199}Hg. Note that, similarly to the case of I [23], the PNC signals for the two hyperfine groups $F = 1/2 \rightarrow F' = 1/2$ and $F = 1/2 \rightarrow F' = 3/2$ deviate in opposite directions, a signature that serves as an important experimental check.

2. Xe

In Fig. 6 the theoretical simulations for the expected PNC rotation signals for metastable Xe are presented. In the simulations presented in Fig. 6(a) we assume densities of $\rho = 1 \times 10^{12}$ cm^{-3} for ^{136}Xe, which can be produced in a discharge lamp. The Doppler width is $\Gamma_D \simeq 2\pi \times 192$ MHz (300 K) and the Lorentz width $\Gamma_L \simeq 2\pi \times 60$ MHz, based on preliminary measurements on a low-pressure He-Xe discharge lamp performed in our laboratory and on measurements presented in Ref. [49]. Assuming $l_{eff} = 150 \times 10^4$ cm, we calculate column densities that correspond to 12 absorption lengths at the center of the absorption. Figure 6(b) shows the PNC optical-rotation signal for the case of pure ^{129}Xe (with nuclear spin $I = 1/2$) demonstrating a resolved hyperfine structure. Assuming the same density and Doppler and Lorentz widths as in the simulations for the ^{136}Xe, we obtain column densities that correspond to 7 absorption lengths (at maximum absorption). Similarly to Hg, we set $\varkappa = 1$ to see the experimental sensitivity to NSD effects. Using the values from Ref. [34], we obtain a total signal difference of up to $\sim 6.2\%$. As the actual value of $\varkappa$ is again expected to be ~ 0.1 (Xe has an odd-neutron nucleus), an experimental precision of
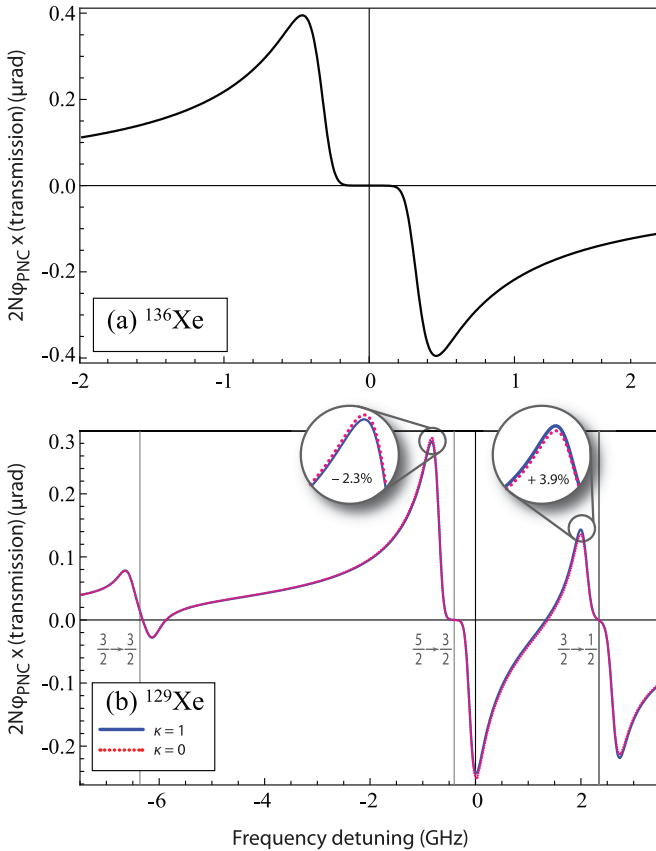
FIG. 6. (Color online) Theoretical prediction of the PNC optical-rotation signal for metastable Xe vs optical frequency assuming (a) a discharge lamp filled with isotopically pure metastable ^{136}Xe producing densities $\rho = 10^{12}$ cm^{-3} and (b) a discharge lamp filled with isotopically pure odd-isotope ^{129}Xe, producing densities of $\rho = 5 \times 10^{12}$ cm^{-3}. The inset shows the full hyperfine structure of the transition (the hyperfine-structure values were taken from Refs. [44–46]). The effect of the nuclear anapole moment is presented, setting $\varkappa = 1$ to yield visibly large signal differences. In both cases we assume transitional Lorentz contributions of $\Gamma_L = 2\pi \times 100$ MHz. See the text for a detailed discussion. All values were taken from Ref. [34].

about 0.1% (6σ precision) is required to measure the nuclear anapole moment in Xe.

In addition, Hg and Xe have large distributions of stable isotopes ($\Delta N/N = 8/120$ and $12/76$, respectively). Ratios of atomic PNC measurements along an isotope chain of the same element can exclude large errors associated with atomic-structure effects [19] and are sensitive to variations in the neutron distribution [20,24].

3. ^{127}I

In Ref. [23], investigations of the expected PNC optical-rotation signal in the 1315-nm transition in ^{127}I were presented. Here we explore further the range of experimental conditions, for which a measurable PNC optical-rotation signal is achievable. In Fig. 7 we present the maximum (peak) PNC optical-rotation angle as a function of the Lorentzian broadening of the line and the average number of passes N (proportional to the finesse of the cavity) for two different
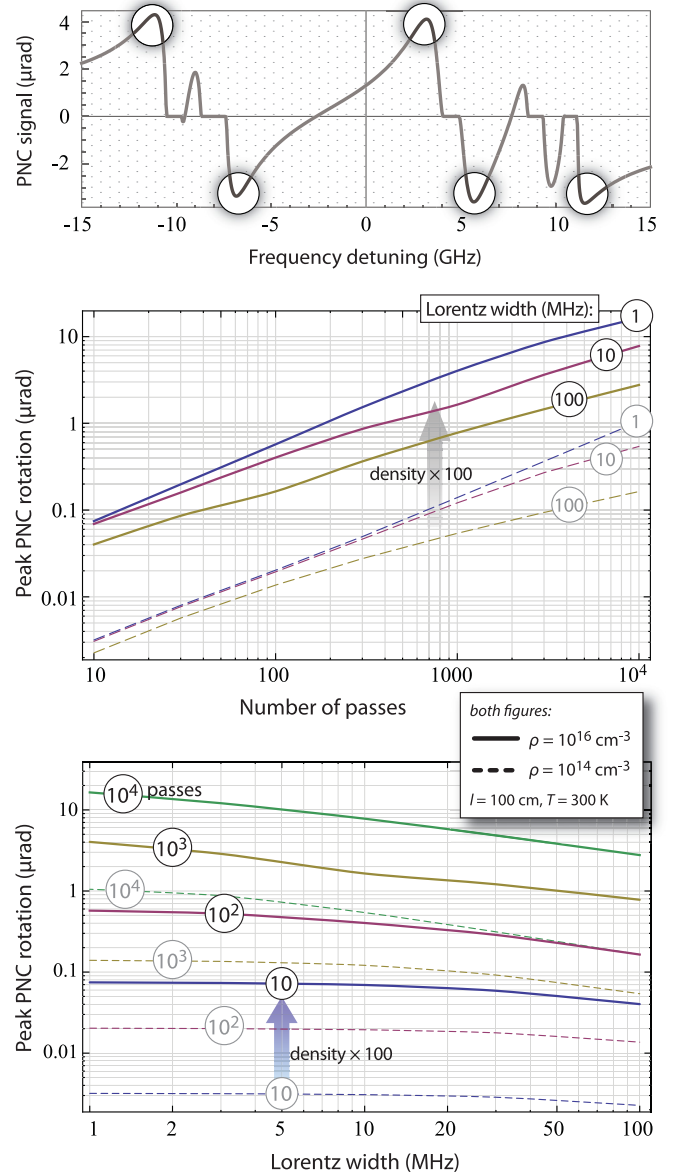

FIG. 7. (Color online) Shown on the top is the theoretical prediction of the PNC optical-rotation signal for the $^2P_{3/2} \rightarrow {}^2P_{1/2}$ transition in ^{127}I (we assume a column density of $\rho l = 1.75 \times 10^{21}$ cm^{-2} and $\Gamma_L = 2\pi \times 3$ MHz). The hyperfine-structure values were taken from Ref. [47]. Shown on the bottom and in the middle are calculations of the maximum (peak) PNC optical-rotation angle as a function of the Lorentzian broadening of the line and the average number of passes N (proportional to the finesse of the cavity), respectively. The simulations are performed for two different extreme-case densities $\rho = 10^{14}$ and 10^{16} cm^{-3}, assuming constant interaction path length and temperature ($\Gamma_D = 2\pi \times 151$ MHz). The nonsmooth features in the simulations are the result of the fact that the peak rotation is not always associated with the same hyperfine component, but switches between hyperfine components (depicted by black circles in the top figure).

extreme-case densities $\rho = 10^{14}$ and 10^{16} cm^{-3} (the former is the minimum density needed to produce observable PNC signals and the latter is arguably the largest that can be produced using the photodissociation method [23]). Note that

the peak optical rotation is not always associated with the same hyperfine component, but switches between hyperfine components depending on the experimental conditions. This peak switching is responsible for the kinks present in the curves of Fig. 7. Finally, we propose the production of these densities from the photodissociation of I_2 with 532-nm radiation (see relevant discussion in Ref. [23]).

Using the values presented in Fig. 7, we see that for densities of $\rho = 10^{16}$ cm^{-3}, a Lorentzian contribution of $\Gamma_L = 2\pi \times 10$ MHz, and an average number of passes of 400, a peak φ_{PNC}^{max} optical-rotation angle of ~ 1 μ rad is expected. Setting $\varkappa = 1$, we predict NSD-PNC signal differences of $\sim 8.5\%$. Using the previously measured values of κ for Cs [5] as the expected value for the anapole moment in iodine [$\varkappa(^{127}\mathrm{I}) \simeq -\varkappa(^{133}\mathrm{Cs}) \simeq -0.38(6)$], we see that a measurement of about $\sim 0.5\%$ sensitivity, corresponding to a 5-nrad detection sensitivity, is required to measure the NSD-PNC effects in $^{127}\mathrm{I}$ with a 6σ precision (see also discussion in Ref. [23]).

VI. CONCLUSION

In this article we presented the fundamental elements of a cavity-enhanced polarimetric measurement of PNC optical rotation. The polarization eigenstates of a four-mirror bow-tie cavity supporting counterpropagating beams were presented. We demonstrated how an absolute measurement of the PNC optical rotation is possible even in the presence of linear birefringence. The measurement procedure and the availability of robust subtraction procedures using two distinct signal reversals were also discussed. Furthermore, theoretical simulations for the expected PNC optical-rotation signals, utilizing the cavity-enhanced optical-rotation technique under experimentally feasible parameters, were presented. These suggest that, for the proposed systems and experimental conditions, measurements of odd-neutron and odd-proton NSD-PNC effects are experimentally feasible. In addition, all the proposed systems are suitable for PNC measurements along a chain of isotopes, particularly Xe, which has the largest distribution of stable isotopes. Finally, we demonstrated that particularly for the case of $^{127}\mathrm{I}$, large optical-rotation signals are expected. We argued that the proposed experimental conditions, as well as the corresponding expected signal values and detection sensitivities for the proposed transition in iodine, compare favorably with those of successful PNC optical-rotation experiments [11–13], suggesting that iodine is the most favorable candidate for future PNC optical-rotation experiments, currently pursued in our laboratory.

ACKNOWLEDGMENTS

APPENDIX A: LINE SHAPES

In the absence of inhomogeneous broadening mechanisms and for frequency detunings much smaller than the resonance frequency $|\omega - \omega_0| \ll \omega_0$, the dispersive and absorptive parts of the line-shape function take the familiar Lorentzian form

$$\mathcal{L}'(\omega - \omega_0) = \frac{1}{\pi} \frac{\omega - \omega_0}{(\omega - \omega_0)^2 + (\Gamma/2)^2}, \quad \text{(A1)}$$

$$\mathcal{L}''(\omega - \omega_0) = \frac{1}{\pi} \frac{\Gamma/2}{(\omega - \omega_0)^2 + (\Gamma/2)^2}, \quad \text{(A2)}$$

where Γ is the full width at half maximum of the Lorentzian line shape. In a thermal vapor the Doppler broadening of the transition due to the motion of the atoms cannot be neglected. The natural way to include it would be to substitute the frequency variable ω by its Doppler shifted value $\omega - \mathbf{k} \cdot \boldsymbol{v}$, where $\mathbf{k}$ is the wave number and $\boldsymbol{v}$ the atomic velocity, and integrate the Lorentzians over a Maxwell velocity distribution, thus arriving at what is known as the Voigt profile. However, this convolution of a Lorentzian with a Gaussian distribution is, for computational purposes, more conveniently expressed through the Faddeeva function $w(z)$, which is a scaled complementary error function of a complex variable $z = x + iy$:

$$w(z) = e^{-z^2}\mathrm{erfc}(-iz) = w'(x,y) + i\, w''(x,y). \quad \text{(A3)}$$

For an atom of mass M and for a transition centered at ω_0, the Doppler half-width at $1/e$ is

$$\Delta\omega_D = \omega_0 \sqrt{\frac{2k_B T}{Mc^2}}, \quad \text{(A4)}$$

where k_B is the Boltzmann constant, c is the speed of light, and T is the vapor temperature. The absorptive and dispersive parts of the line shape are related to the real w' and imaginary w'' parts of the Faddeeva function, respectively, via

$$\mathcal{L}''(\omega - \omega_0) \rightarrow \mathcal{V}''(\omega - \omega_0) = \frac{w'\left(\frac{\omega - \omega_0}{\Delta\omega_D}, \frac{\Gamma/2}{\Delta\omega_D}\right)}{\sqrt{\pi}\,\Delta\omega_D}, \quad \text{(A5)}$$

$$\mathcal{L}'(\omega - \omega_0) \rightarrow \mathcal{V}'(\omega - \omega_0) = \frac{w''\left(\frac{\omega - \omega_0}{\Delta\omega_D}, \frac{\Gamma/2}{\Delta\omega_D}\right)}{\sqrt{\pi}\,\Delta\omega_D}. \quad \text{(A6)}$$

APPENDIX B: INDEX OF REFRACTION

1. Electric quadrupole interaction $E2$

In our proposed transitions for Xe, Hg, and I (with the exception of the $^3P_0^o \rightarrow {}^1P_1^o$ transition in Hg) selection rules allow for the existence of an electric quadrupole interaction that must be included. The electric quadrupole operator for the $\eta = \pm 1$ component of circular polarization (with the positive sign denoting left-circularly polarized light) is

$$-\frac{\eta\omega}{4\sqrt{3}}Q_\eta^{(2)} \quad \text{for} \quad Q_\eta^{(2)} = -2er^2\sqrt{4\pi/5}Y_\eta^{(2)}, \quad \text{(B1)}$$

where $Y_\eta^{(2)}$ is a spherical harmonic function [61]. Inclusion of the $E2$ electric quadrupole amplitude to the index of refraction

(in addition to the inclusion of the $E1_{\text{PNC}}$ dipole amplitude) is performed by the substitution in Eq. (4):

$$\frac{M_1^2}{3} \to |\langle J \| i d^{(1)} + \mu^{(1)} - \frac{\omega}{4\sqrt{3}} Q^{(2)} \| J' \rangle|^2. \quad (B2)$$

Introducing the electric quadrupole to magnetic dipole ratio parameter χ,

$$\chi = \frac{\omega}{4\sqrt{3}} \frac{\langle J \| Q^{(2)} \| J' \rangle}{\langle J \| \mu^{(1)} \| J' \rangle}, \quad (B3)$$

and using (assuming that space is isotropic)

$$\langle J \| T_\eta^{(k)} \| J' \rangle = \frac{1}{2k+1} \langle J \| T^{(k)} \| J' \rangle \quad (B4)$$

(where $T_\eta^{(k)}$ is the ηth component of the rank-k tensor T), we arrive at [by use of Eq. (5)]

$$n = 1 + n_0 \sum_{F,F'} C'_{FF'} \mathcal{V}_{FF'}(\omega), \quad (B5)$$

the difference with Eq. (7) being the $C_{FF'} \to C'_{FF'}$ substitution with

$$C'_{FF'} = \frac{(2F+1)(2F'+1)}{2I+1}$$
$$\times \left(\begin{Bmatrix} J & 1 & J' \\ F' & I & F \end{Bmatrix}^2 + \frac{3\chi^2}{5} \begin{Bmatrix} J & 2 & J' \\ F' & I & F \end{Bmatrix}^2 \right). \quad (B6)$$

Note that no interference term between the electric quadrupole and PNC dipole interactions appears, as it cancels out when one explicitly performs the summation across the magnetic sublevels before reducing the matrix elements.

2. Accounting for isotopes

In the case where the studied vapor comprises more than one isotope, each with an abundance b_i, the index of refraction will just be the sum of the refractive indices for each isotope n_i weighted by their respective abundances:

$$n = \sum_i b_i n_i. \quad (B7)$$

The central difference among the various n_i is in the resonance frequency $\omega_{FF'} \to \omega_{FF',i}$. Each isotope has an *isotope-shifted* resonance frequency, stemming from the slight variations in the electron wave functions due to the different nuclear masses. This is the only difference for even isotopes that have no nuclear spin, hence $F(F') \to J(J')$ and $\omega_{FF',i} \to \omega_{JJ',i}$. For odd isotopes, the nonzero nuclear spin causes the appearance of hyperfine structure with different ground- and excited-state hyperfine constants for each odd isotope. It is then $\omega_{FF',i} = \omega_{JJ'} + \delta\omega_i + \Delta\omega_{F',i}^{(\text{hf})} - \Delta\omega_{F,i}^{(\text{hf})}$, with

$$\Delta\omega_F^{(\text{hf})} = \frac{1}{2} A^{(\text{hf})} K + B^{(\text{hf})} \frac{\frac{3}{2} K(K+1) - 2I(I+1)J(J+1)}{I(I-1)(2I-1)J(J-1)(2J-1)}$$
$$\text{for} \qquad K = F(F+1) - I(I+1) - J(J+1), \quad (B8)$$

where $A^{(\text{hf})}$ and $B^{(\text{hf})}$ are the magnetic dipole and electric quadrupole hyperfine constants, respectively, and $\delta\omega_i$ is the isotope shift. Other affected quantities are the Doppler width (which is proportional to $1/\sqrt{M_i}$ and is taken into account in the calculations) and the reduced matrix elements (where changes are generally very small).

[1] Ya. B. Zel'dovich, Zh. Eksp. Teor. Fiz. **36**, 964 (1959) [Sov. Phys. JETP **9**, 682 (1959)].

[2] M. A. Bouchiat and C. Bouchiat, Phys. Lett. **48B**, 111 (1974).

[3] R. Diener, S. Godfrey, and I. Turan, Phys. Rev. D **86**, 115017 (2012).

[4] J. S. M. Ginges and V. V. Flambaum, Phys. Rep. **397**, 63 (2004).

[5] C. S. Wood, S. C. Bennett, D. Cho, B. P. Masterson, J. L. Roberts, C. E. Tanner, and C. E. Wieman Science **275**, 1759 (1997).

[6] K. Tsigutkin, D. Dounas-Frazer, A. Family, J. E. Stalnaker, V. V. Yashchuk, and D. Budker, Phys. Rev. Lett. **103**, 071601 (2009).

[7] A. T. Nguyen, D. Budker, D. DeMille, and M. Zolotorev, Phys. Rev. A **56**, 3453 (1997).

[8] M.-A. Bouchiat, Phys. Rev. Lett. **100**, 123003 (2008).

[9] D. Sheng, L. A. Orozco, and E. Gomez, J. Phys. B **43**, 074004 (2010).

[10] V. A. Dzuba, V. V. Flambaum, and B. Roberts, Phys. Rev. A **86**, 062512 (2012).

[11] P. A. Vetter, D. M. Meekhof, P. K. Majumder, S. K. Lamoreaux, and E. N. Fortson, Phys. Rev. Lett. **74**, 2658 (1995).

[12] M. J. D. Macpherson, K. P. Zetie, R. B. Warrington, D. N. Stacey, and J. P. Hoare, Phys. Rev. Lett. **67**, 2784 (1991).

[13] D. M. Meekhof, P. Vetter, P. K. Majumder, S. K. Lamoreaux, and E. N. Fortson, Phys. Rev. Lett. **71**, 3442 (1993).

[14] J. A. Sherman, T. W. Koerber, A. Markhotok, W. Nagourney, and E. N. Fortson, Phys. Rev. Lett. **94**, 243001 (2005).

[15] L. W. Wansbeek, B. K. Sahoo, R. G. E. Timmermans, K. Jungmann, B. P. Das, and D. Mukherjee, Phys. Rev. A **78**, 050501 (2008).

[16] M. Nuñez Portela, J. E. van den Berg, H. Bekker, O. Böll, E. A. Dijck, G. S. Giri, S. Hoekstra, K. Jungmann, A. Mohanty, C. J. G. Onderwater, B. Santra, S. Schlesser, R. G. E. Timmermans, O. O. Versolato, L. W. Wansbeek, L. Willmann, and H. W. Wilschut, Hyperfine Interact. **214**, 157 (2013).

[17] V. G. Gorshkov, V. F. Ezhov, M. G. Kozlov, and A. I. Mikhailov, Sov. J. Nucl. Phys. **48**, 1363 (1988).

[18] E. Gomez, L. A. Orozco, and G. D. Sprouse, Rep. Prog. Phys. **69**, 79 (2006).

[19] V. A. Dzuba, V. V. Flambaum, and I. B. Khriplovich, Z. Phys. D **1**, 243 (1986).

[20] E. N. Fortson, Y. Pang, and L. Wilets, Phys. Rev. Lett. **65**, 2857 (1990).

[21] D. DeMille, S. B. Cahn, D. Murphree, D. A. Rahmlow, and M. G. Kozlov, Phys. Rev. Lett. **100**, 023003 (2008).

[22] L. Bougas, G. E. Katsoprinakis, W. von Klitzing, J. Sapirstein, and T. P. Rakitzis, Phys. Rev. Lett. **108**, 210801 (2012).

[23] G. E. Katsoprinakis, L. Bougas, T. P. Rakitzis, V. A. Dzuba, and V. V. Flambaum, Phys. Rev. A **87**, 040101(R) (2013).

[24] B. A. Brown, A. Derevianko, and V. V. Flambaum, Phys. Rev. C **79**, 035501 (2009).

[25] G. J. Roberts, P. E. G. Baird, M. W. S. M. Brimicombe, P. G. H. Sandars, D. R. Selby, and D. N. Stacey, J. Phys. B **13**, 1389 (1980).

[26] P. A. Vetter, Ph.D. thesis, University of Washington, 1995.

[27] I. I. Sobel'man, *Atomic Spectra and Radiative Transitions* (Springer, Berlin, 1979).

[28] J. T. Verdeyen, *Laser Electronics*, 3rd ed. (Prentice-Hall, Englewood Cliffs, 1995).

[29] A. A. Papchenko and E. A. Yukov, J. Russ. Laser Res. **15**, 493 (1994).

[30] P. Siddons, Ph.D. thesis, Durham University, 2011.

[31] G. T. Purves, Ph.D. thesis, Durham University, 2006.

[32] G. E. Katsoprinakis, Ph.D. thesis, University of Crete, 2010.

[33] D. A. Steck, Los Alamos National Laboratory Report No. LA-UR-03-8638 (2008).

[34] V. A. Dzuba and V. V. Flambaum, Phys. Rev. A **86**, 052512 (2012).

[35] E. N. Fortson and L. L. Lewis, Phys. Rep. **113**, 289 (1984).

[36] V. N. Novikov, O. P. Sushkov, V. V. Flambaum, and I. B. Khriplovich, Zh. Eksp. Teor. Fiz. **73**, 802 (1977) [Sov. Phys. JETP **46**, 420 (1977)].

[37] V. V. Flambaum and I. B. Khriplovich, Zh. Eksp. Teor. Fiz. **79**, 1656 (1980) [Sov. Phys. JETP **52**, 835 (1980)].

[38] V. V. Flambaum and I. B. Khriplovich, Zh. Eksp. Teor. Fiz. **89**, 1505 (1985) [Sov. Phys. JETP **62**, 872 (1985)].

[39] V. V. Flambaum, I. B. Khriplovich, and O. P. Sushkov, Phys. Lett. **146B**, 367 (1984).

[40] V. V. Flambaum and I. B. Khriplovich, Phys. Lett. **110A**, 121 (1985).

[41] V. V. Flambaum and D. W. Murray, Phys. Rev. C **56**, 1641 (1997).

[42] T. S. Subbaraya and T. G. Srinivasa Iyengar, Proc. R. Soc. London Ser. A **137**, 216 (1932).

[43] R. H. Kohler, Phys. Rev. **121**, 1104 (1960).

[44] G. D Amico, G. Pesce, and A. Sasso, Hyperfine Interact. **127**, 121 (2000).

[45] W. Fischer, H. Huhnermann, G. Kroemer, and H. J. Schafer, Z. Phys. **270**, 113 (1974).

[46] M. Walhout, H. J. L. Megens, A. Witte, and S. L. Rolston, Phys. Rev. A **48**, R879 (1993).

[47] R. Engleman, Jr., R. A. Keller, and B. A. Palmer, Appl. Opt. **19**, 2767 (1980).

[48] J. J. Curry, G. G. Lister, and J. E. Lawler, J. Phys. D **35**, 2945 (2002).

[49] R. Bussiahn, G. Gortchakov, H. Lange, and D. Uhrlandt, J. Appl. Phys. **95**, 4627 (2004).

[50] W. Happer, Rev. Mod. Phys. **44**, 169 (1972).

[51] M. Durand, J. Morville, and D. Romanini, Phys. Rev. A **82**, 031803 (2010).

[52] J. Poirson, M. Vallet, F. Bretenaker, A. L. Floch, and J. Thepot, Anal. Chem. **70**, 4636 (1998).

[53] R. C. Jones, J. Opt. Soc. Am. **31**, 488 (1941); **31**, 493 (1941); **31**, 500 (1941).

[54] T. Muller, K. B. Wiberg, P. H. Vaccaro, J. R. Cheeseman, and M. J. Frischand, J. Opt. Soc. Am. B **19**, 125 (2002).

[55] A. C. Nilsson, E. K. Gustafson, and R. L. Byer, IEEE J. Quantum Electron. **25**, 767 (1989).

[56] J. L. Hall, J. Ye, and L.-S. Ma, Phys. Rev. A **62**, 013815 (2000).

[57] D. Budker, W. Gawlik, D. F. Kimball, S. M. Rochester, V. V. Yashchuk, and A. Weis, Rev. Mod. Phys. **74**, 1153 (2002).

[58] R. W. P. Drever, J. L. Hall, F. V. Kowalski, J. Hough, G. M. Ford, A. J. Munley, and H. Ward, Appl. Phys. B **31**, 97 (1983).

[59] H. G. Berry, G. Gabrielse, and A. E. Livingston, Appl. Opt. **16**, 3200 (1977).

[60] C. J. Hood, H. J. Kimble, and J. Ye, Phys. Rev. A **64**, 033804 (2001).

[61] R. N. Zare, *Angular Momentum: Understanding Spatial Aspects in Physics and Chemistry* (Wiley Interscience, New York, 1987).